

Semi-Supervised Learning for AVO Inversion with Strong Spatial Feature Constraints

Yingtian Liu, Yong Li, Junheng Peng, and Mingwei Wang

Abstract—One-dimensional convolution is a widely used deep learning technique in prestack amplitude variation with offset (AVO) inversion; however, it lacks lateral continuity. Although two-dimensional convolution improves lateral continuity, due to the sparsity of well-log data, the model only learns weak spatial features and fails to explore the spatial correlations in seismic data fully. To overcome these challenges, we propose a novel AVO inversion method based on semi-supervised learning with strong spatial feature constraints (SSFC-SSL). First, two-dimensional predicted values are obtained through the inversion network, and the predicted values at well locations are sparsely represented using well-log labels. Subsequently, a label-annihilation operator is introduced, enabling the predicted values at non-well locations to learn the spatial features of well locations through the neural network. Ultimately, a two-way strong spatial feature mapping between non-well locations and well locations is achieved. Additionally, to reduce the dependence on well-log labels, we combine the semi-supervised learning strategy with a low-frequency model, further enhancing the robustness of the method. Experimental results on both synthetic example and field data demonstrate that the proposed method significantly improves lateral continuity and inversion accuracy compared to one- and two-dimensional deep learning techniques.

Index Terms—prestack amplitude variation with offset (AVO) inversion, semi-supervised learning, strong spatial feature constraints.

I. INTRODUCTION

AMPLITUDE variation with offset (AVO) analysis has long been a crucial tool in hydrocarbon exploration and reservoir characterization, providing valuable insights into the elastic properties of subsurface formations [1], [2], [3]. Zoeppritz [4] conducted the first theoretical investigation into AVO technology. By examining the variation in reflection coefficients with incidence angles, he analyzed the parameter changes in the media on either side of the reflection interface and formulated the Zoeppritz equations. Although these equations provide precise calculations of reflection coefficients, their complex expressions make them challenging to apply directly to AVO inversion of real-world data. Consequently, researchers have developed simplified versions of the Zoeppritz equations from various perspectives [5], [6], [7], [8], [9], [10].

Model-driven AVO inversion is a method to extract seismic parameters such as P-wave velocity, S-wave velocity, and

density from prestack seismic data based on AVO theory. The traditional model-driven AVO inversion method used a linear method to establish the mapping between the reflection coefficient and parameters. Ikelle [11] proposed a linear AVO inversion algorithm based on the least-squares method for processing 3D multi-migration seismic data. Downton and Ursenbach [12] proposed a linearized AVO inversion method that can accurately deal with the reflection coefficients of the above critical angles, considering the amplitude and phase changes with the migration. However, AVO inversion is an ill-posed problem with many difficulties, such as limited data bandwidth, noise corruption, and incomplete data coverage [13], [14]. To overcome this problem, many methods have been proposed, including Bayesian probabilistic inversion [15], [16], exhaustive searching [17], [18]. Gradient-based algorithms, such as the limited-memory BFGS (L-BFGS) method [19], [20], are commonly employed for nonlinear inverse problems. These techniques typically involve the construction of a geological or petrophysical model, which is then used to derive synthetic seismic responses that are matched to the observed data through an iterative optimization process [21], [22], [23]. While these inversion methods have demonstrated promising results, they are computationally intensive, and their outcomes are highly sensitive to the selection of the initial model [24], [25], [26].

Deep learning (DL), known for its ability to represent complex features and perform nonlinear mapping, has become a key research focus in seismic exploration [27], [28]. In this field, DL techniques have achieved promising results in various aspects, including reservoir parameter prediction [29], [30], fault identification [31], [32], noise attenuation [33], [34], and stratigraphic interpretation [35], [36]. In recent years, DL has also been developed in AVO inversion. Das et al. [37] employed a one-dimensional convolutional neural network (CNN) for seismic inversion. Mustafa et al. [38] proposed a workflow for impedance prediction utilizing temporal convolutional networks (TCN). Cao et al. [39] proposed a DL-based AVO inversion method with Dropout regularization, enhancing the prediction accuracy and stability of P-wave velocity, S-wave velocity, and density. As shown in Fig. 1(a), the earliest DL inversion method was to extract the characteristics of prediction parameters from single-trace seismic data and utilize well-log data to constrain these characteristics, thereby establishing a non-linear mapping between seismic data and elastic parameters. [40], [41], [42].

In practical applications, the availability of labeled data is limited due to the high cost of well-log data. To solve the challenge of limited labeled data, scholars have introduced

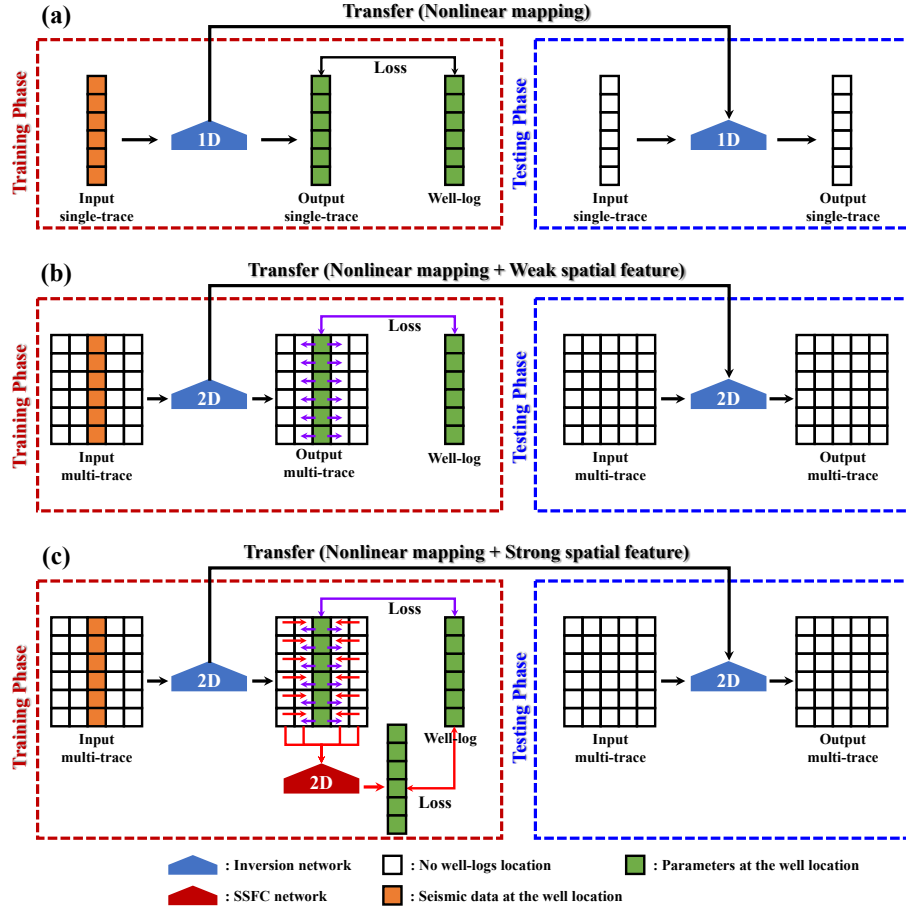


Fig. 1. Training and testing workflows for seismic inversion methods. (a) 1D data-driven seismic inversion, (b) 2D data-driven seismic inversion, and (c) the SSFC-SSL seismic inversion method.

various constraints. Alfarraj and AlRegib [43] proposed a semi-supervised recurrent neural network (RNN) framework based on seismic forward modeling. Liu et al. [44] integrated the semi-supervised temporal convolutional network with Nash game theory [45] to effectively address the gradient conflict problem in AVO inversion. Physics-guided neural networks (PGNN) have also been applied to both prestack and post-stack AVO inversion [46], [47], [48]. Many semi-supervised inversion methods incorporating model-based forward modeling have been developed to address various geological inverse problems [49], [50], [51]. These methods incorporate seismic data constraints through model-based forward modeling but depend on the precise determination of the wavelet, which is challenging in practical applications. Yuan et al. [52] proposed employing a network as an alternative to the traditional physical forward modeling process. Shi et al. [53] introduced a closed-loop seismic inversion method that incorporates a forward network to constrain the inversion network. Wang et al. [54] proposed an AVO inversion method based on the closed-loop seismic inversion framework, capable of accurately inverting the P-wave velocity, S-wave velocity, and density. Although these methods effectively establish the mapping between single-trace seismic data and corresponding single-trace parameters, they overlook the spatial correlations

among the traces, resulting in significant vertical artifacts in the inversion results.

To improve lateral continuity, high-dimensional convolutional kernels were introduced to establish correlations between multi-trace seismic data and multi-trace parameters. Wu et al. [55] proposed an improved DL method based on two-dimensional CNN that significantly improves the stability of impedance prediction. Wang et al. [56] introduced a two-dimensional semi-supervised inversion method that improves the accuracy and spatial continuity of seismic inversion. Mustafa et al. [57] proposed a joint learning strategy that integrates a two-dimensional temporal convolutional network (TCN) and spatial contexts, improving the robustness and spatial consistency of the estimated parameters. Li et al. [58] developed a three-dimensional residual structure, which is used for efficient 3D seismic impedance inversion. These methods process multi-trace seismic data using high-dimensional convolution kernel and output single-trace prediction parameters. As shown in Fig. 2(b), during training, these methods take multi-trace seismic data as input and produce predicted multi-trace parameters as output. The predicted parameters at well locations are constrained by well-log data. In contrast, those at non-well locations are derived from the sparse representation of well-log information and spatial reasoning facilitated by the

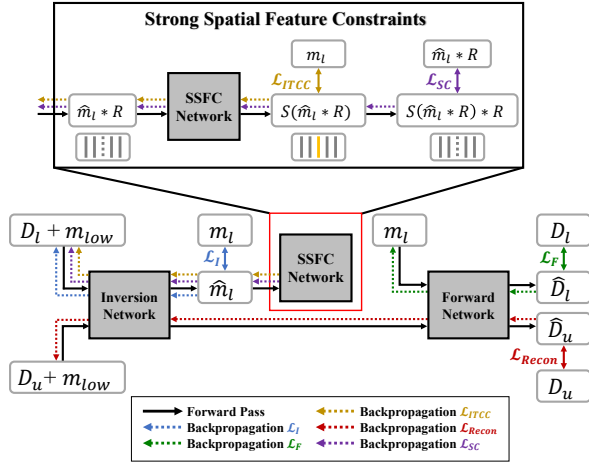


Fig. 2. Training process of SSFC-SSL.

two-dimensional network. Although these methods improve the lateral continuity of the inversion results to some extent, we have observed that they primarily utilize weak one-way spatial correlations from well to non-well locations. Consequently, they fail to capture the stronger spatial features within the seismic data.

To fully explore the strong spatial features in seismic data and improve the accuracy of prestack seismic AVO inversion, we propose a semi-supervised seismic inversion method based on strong spatial feature constraints (SSFC-SSL). SSFC-SSL combines an inversion network, a forward network, and a strong spatial feature constraint (SSFC) network. As shown in Figure 1 (c), multi-trace inputs can yield multi-trace outputs through the inversion network. Specifically, the predicted parameters at well locations undergo feature learning through well-log data, while the parameters at non-well locations are inferred laterally by the network. Subsequently, the predicted parameters at non-well locations are used to infer the parameters at well locations via the SSFC network, thereby establishing a bidirectional strong spatial relationship between well and non-well locations. Additionally, considering the limited number of labels in practice, we constructed a forward-modeling network to make full use of the seismic data at non-well locations and improve the generalization ability of the method.

The article is organized as follows. First, we introduce the theory of SSFC-SSL, including its framework, training workflow, and network structure. Then, we compare the AVO inversion results of the L-BFGS method, the one-dimensional deep learning method, the two-dimensional deep learning method, and the proposed method. Next, the field data application is provided to demonstrate the feasibility of our method for field data. Finally, we draw the key conclusions.

II. THEORY

A. Prestack AVO inversion and forward

AVO is a crucial technique for characterizing subsurface reservoirs by analyzing the variation in seismic wave amplitudes with offset. Its theoretical foundation is the convolution

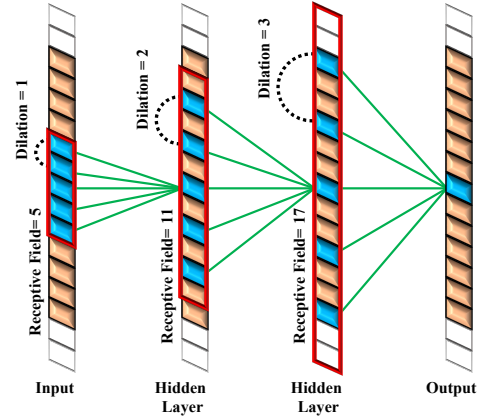


Fig. 3. The structure of dilated convolution.

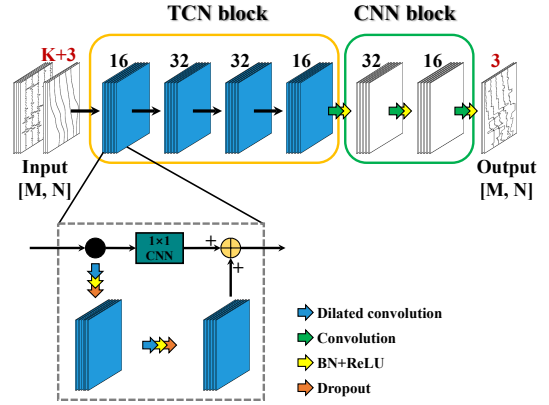


Fig. 4. Architecture of the inversion network.

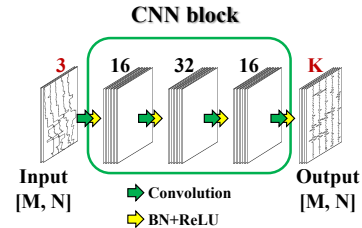


Fig. 5. Architecture of the forward network.

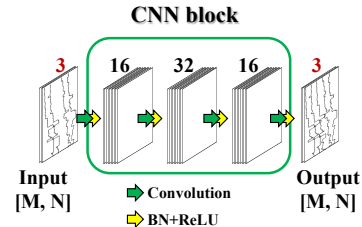


Fig. 6. Architecture of the SSFC network.

model. In the absence of random noise, the convolution model

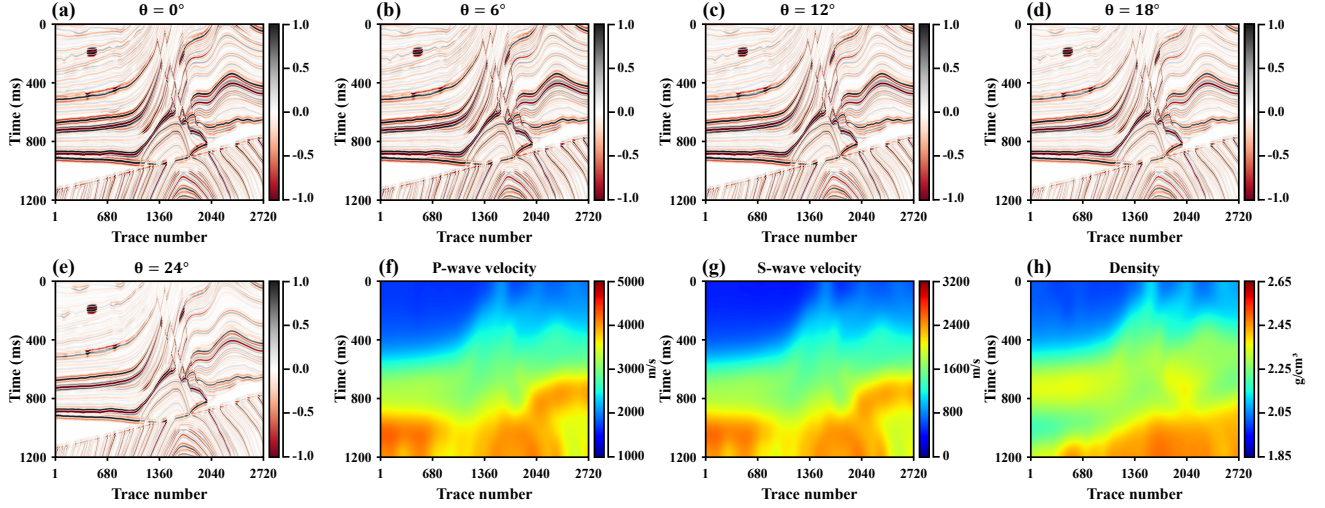


Fig. 7. Synthetic angle gather profiles with different incident angles of (a) 0° , (b) 6° , (c) 12° , (d) 18° , and (e) 24° . Low-frequency information profile of (f) P-wave velocity, (g) S-wave velocity, and (h) density.

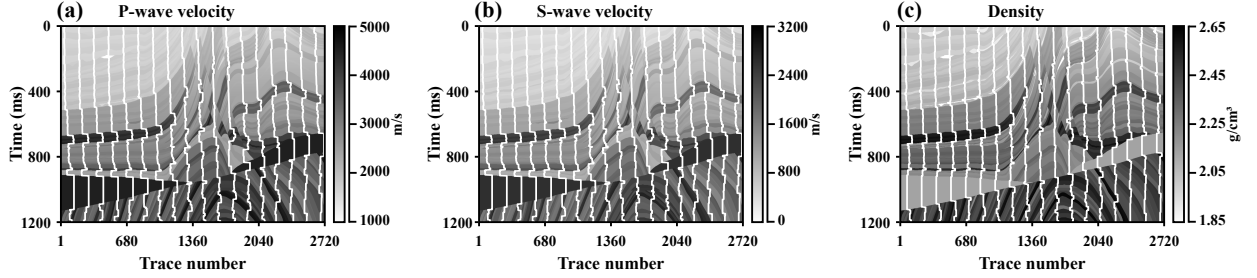


Fig. 8. Training traces of (a) P-wave velocity, (b) S-wave velocity, and (c) density.

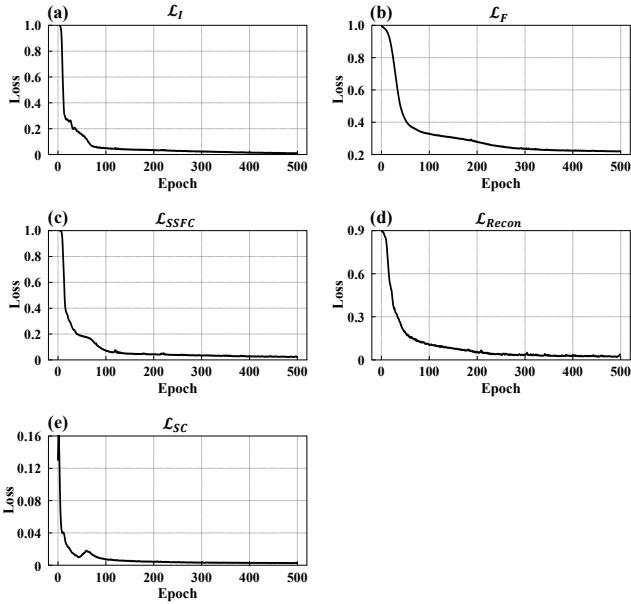


Fig. 9. Loss function curves of (a) \mathcal{L}_I , (b) \mathcal{L}_F , (c) \mathcal{L}_{SSFC} , (d) \mathcal{L}_{Recon} , and (e) \mathcal{L}_{SC} .

TABLE I
HYPERPARAMETERS IN SSFC-SSL.

The type of the hyperparameter		Value
Basic parameter	Epoch	500
	Batch size	100
	Learning rate	0.002
	Weight decay	0.0001
	Dropout	0.2
	Initial kernel size	3
Inversion network	Number of channels of TCN	[16,32,32,16]
	Dilation factor of TCN	[1,2,4,8]
	Number of channels of CNN	[32,16,3]
Forward network	Number of channels of CNN	[16,32,16,5]
SSFC network	Number of channels of CNN	[16,32,16,3]

can be expressed as

$$D = W * R_{PP} \quad (1)$$

where D represents seismic data, represented as the matrix $M * N$, where M denotes the number of traces and N represents the depth of a single trace sequence, f represents the mapping matrix between seismic parameters and reflection coefficients, W is the seismic wavelet, and R_{pp} denotes the

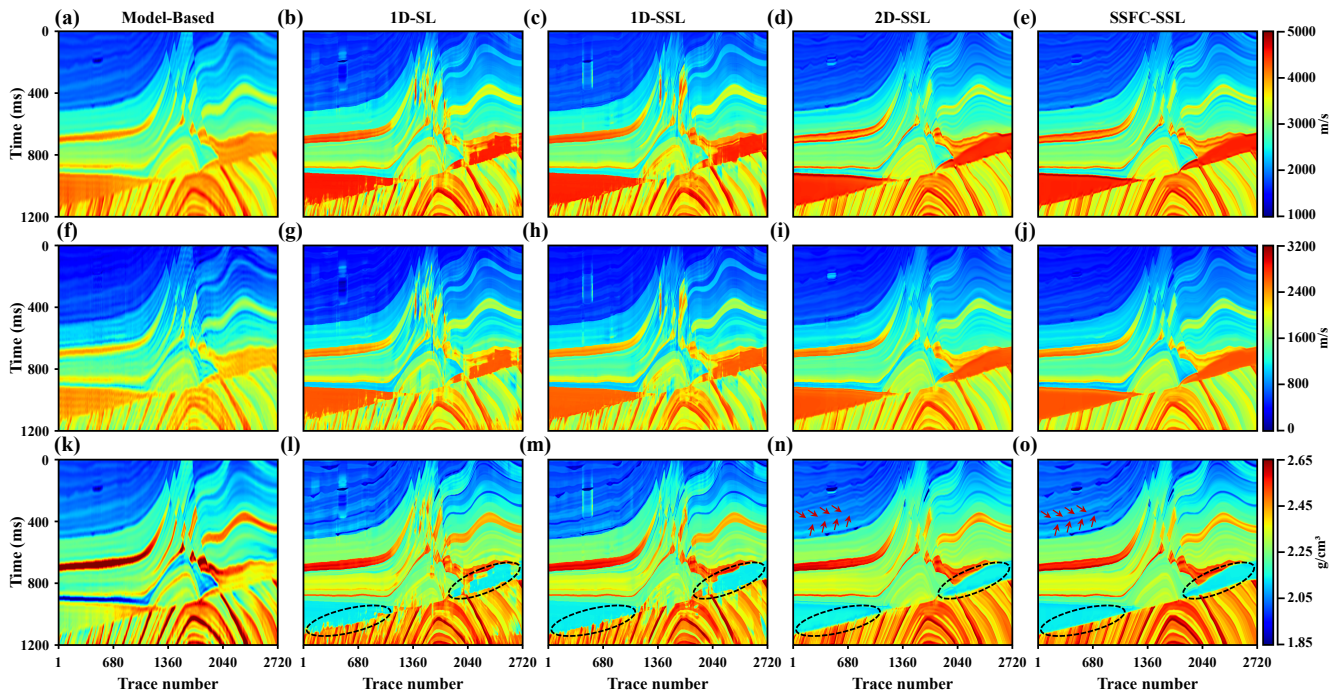


Fig. 10. Inversion results for (a)-(e) P-wave velocity, (f)-(j) S-wave velocity, and (k)-(o) density using different methods. The first column shows the model-based inversion results, the second column shows the 1D-SL inversion results, the third column shows the 1D-SSL inversion results, the fourth column shows the 2D-SSL inversion results, and the last column shows the SSFC-SSL inversion results.

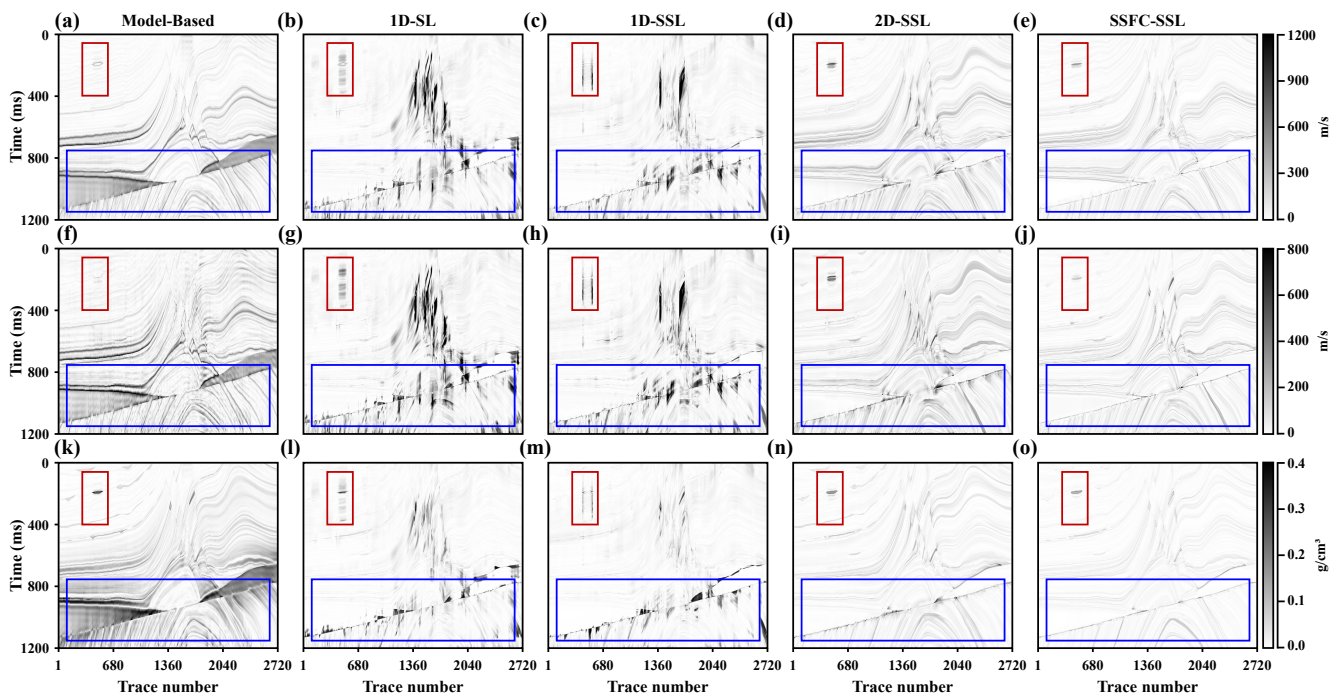


Fig. 11. Absolute difference in (a-e) P-wave velocity, (f-j) S-wave velocity, and (k-o) density inversion results compared to the true data. The figure layout is consistent with Fig. 10.

P-wave reflection coefficient, which is typically a function of velocity, density, and incident angle. Zoeppritz (1919)

proposed equations to describe the reflection and transmission coefficients of PP and PS waves generated when a longitudinal

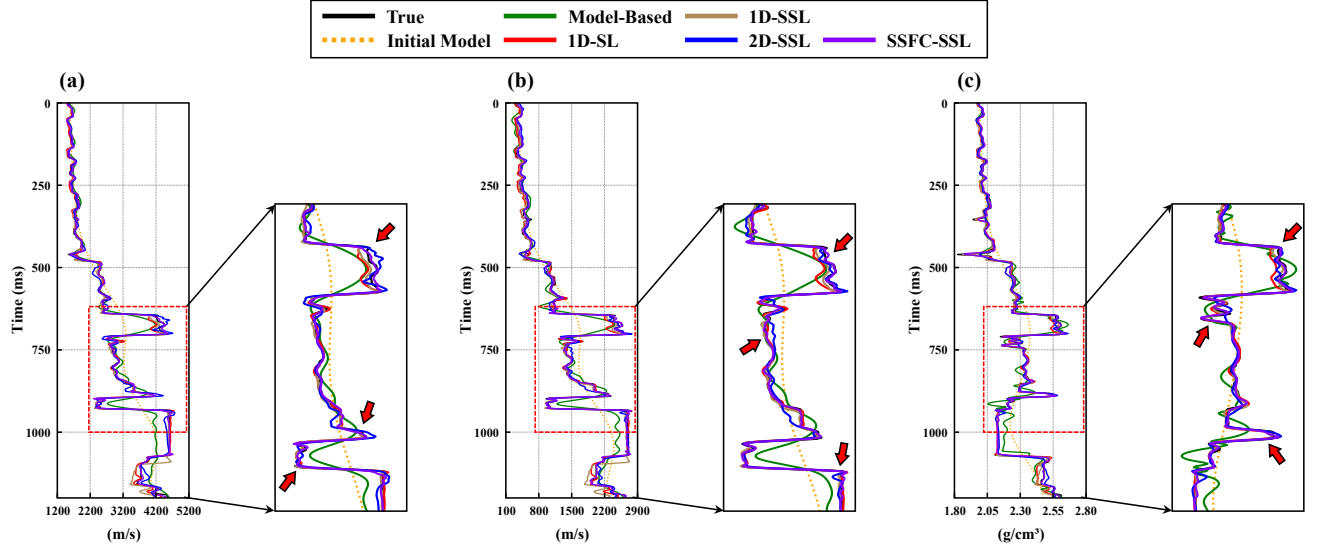


Fig. 12. Inversion results of (a) P-wave velocity, (b) S-wave velocity, and (c) density at trace 600 on the synthetic data. The black lines indicate true data, the orange dotted lines indicate the initial models, the green lines indicate the model-based inversion results, the red lines indicate the 1D-SL inversion results, the brown lines indicate the 1D-SSL inversion results, the blue lines indicate the 2D-SSL inversion results, and the purple lines indicate the SSFC-SSL inversion results.

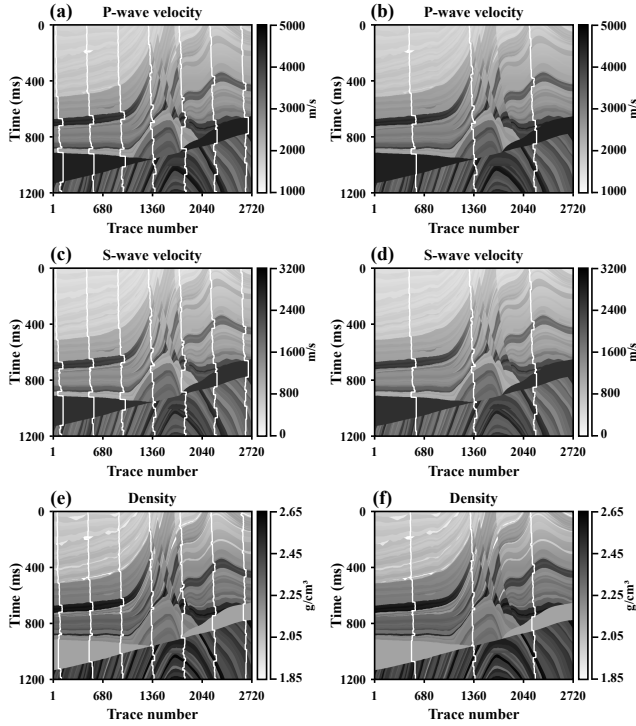


Fig. 13. (a) Seven training traces and (b) three training traces for P-wave velocity; (c) seven training traces and (d) three training traces for S-wave velocity; (e) seven training traces and (f) three training traces for density.

$$\begin{aligned}
 & \begin{bmatrix} R_{PP} \\ R_{PS} \\ T_{PP} \\ T_{PS} \end{bmatrix} \\
 &= \begin{bmatrix} \sin \theta_1 & \cos \varphi_1 & -\sin \theta_2 & \cos \varphi_2 \\ -\cos \theta_1 & \sin \varphi_1 & -\cos \theta_2 & -\sin \varphi_2 \\ \sin 2\theta_1 & \frac{V_{P1}}{V_{S1}} \cos 2\varphi_1 & \frac{\rho_2 V_{S2}^2 V_{P1}}{\rho_1 V_{S1}^2 V_{P2}} \sin 2\theta_2 & \frac{-\rho_2 V_{S2} V_{P1}}{\rho_1 V_{S1}^2} \cos 2\varphi_2 \\ \cos 2\varphi_1 & \frac{-V_{S1}}{V_{P1}} \sin 2\varphi_1 & \frac{-\rho_2 V_{P2}}{\rho_1 V_{P1}} \cos 2\varphi_2 & \frac{-\rho_2 V_{S2}}{\rho_1 V_{P1}} \sin 2\varphi_2 \end{bmatrix}^{-1} \\
 &\times \begin{bmatrix} -\sin \theta_1 \\ -\cos \theta_1 \\ \sin 2\theta_1 \\ -\cos 2\varphi_1 \end{bmatrix}
 \end{aligned} \tag{2}$$

where θ_1 , θ_2 , φ_1 , and φ_2 represent the incident P-wave angle, the transmitted P-wave angle, the reflected S-wave angle, and the transmitted S-wave angle, respectively. V_{P1} , V_{S1} , and ρ_1 represent the P-wave velocity, S-velocity, and density of the medium in the upper layer of the reflective interface, while V_{P2} , V_{S2} , and ρ_2 represent the P-wave velocity, S-wave velocity, and density of the medium in the lower layer. R_{PP} , R_{PS} , T_{PP} , and T_{PS} correspond to the coefficients of the reflected P-wave, reflected S-wave, transmitted P-wave, and transmitted S-wave, respectively. According to Snell's law, the relationship between the incident angle and velocity can be expressed as

wave in an isotropic medium meets a reflective interface. The equations are

$$\frac{\sin \theta_1}{V_{P1}} = \frac{\sin \theta_2}{V_{P2}} = \frac{\sin \varphi_1}{V_{S1}} = \frac{\sin \varphi_2}{V_{S2}} \tag{3}$$

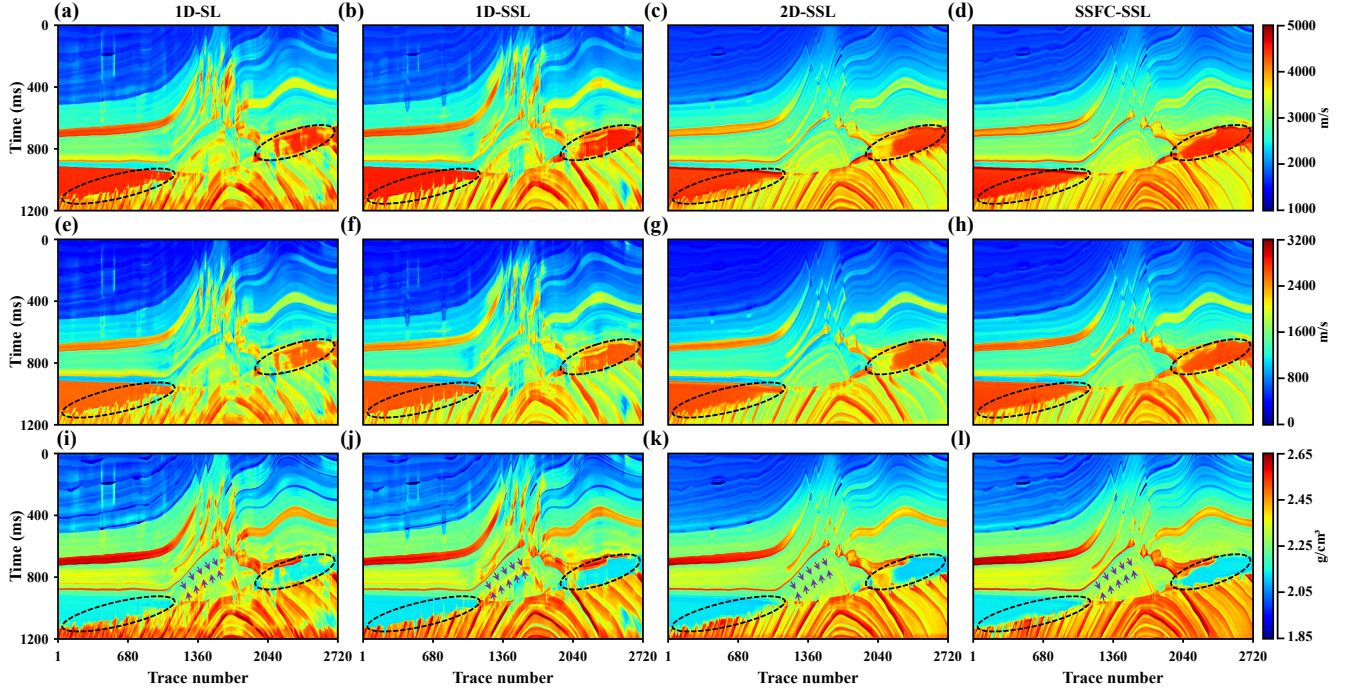


Fig. 14. Inversion results for (a)-(e) P-wave velocity, (f)-(j) S-wave velocity, and (k)-(o) density using different methods with seven training traces. The first column shows the 1D-SL inversion results, the second column shows the 1D-SSL inversion results, the third column shows the 2D-SSL inversion results, and the last column shows the SSFC-SSL inversion results.

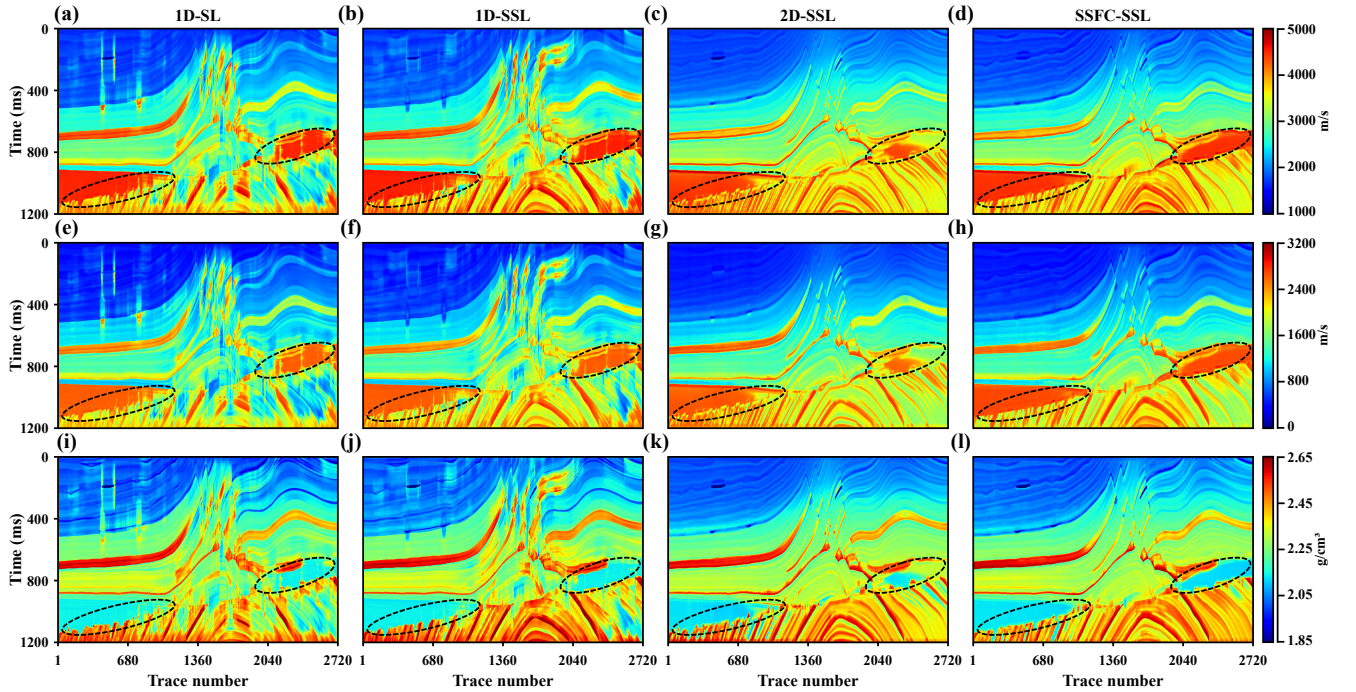


Fig. 15. Inversion results for (a)-(e) P-wave velocity, (f)-(j) S-wave velocity, and (k)-(o) density using different methods with three training traces. The figure layout is consistent with Fig. 14.

By combining equations (3) and (2), the reflection coefficient can be simplified as

$$R_{PP} = f(m) \quad (4)$$

where m is a vector set of elastic parameters: P-wave velocity, S-wave velocity, and density, represented as $m = [V_P, V_S, \rho]$, f represents the mapping matrix between seismic parameters

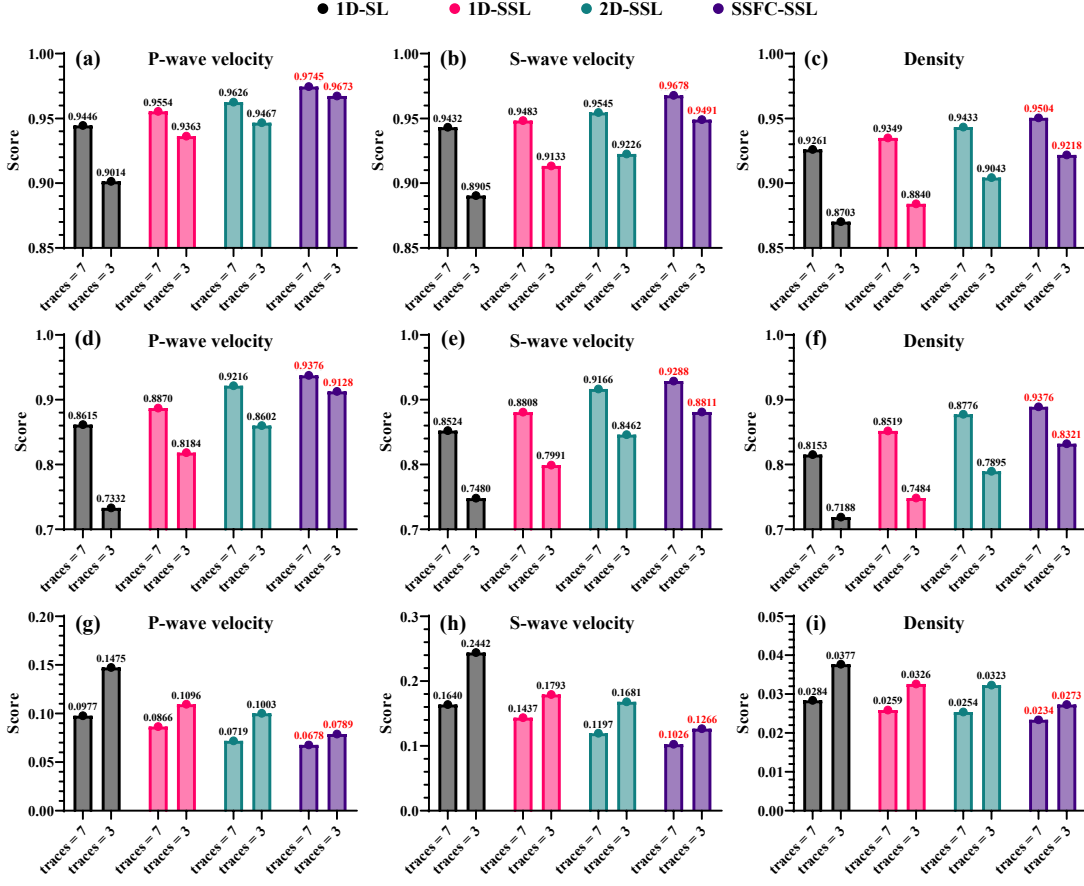


Fig. 16. Comparison of the (a)-(c) PCC, (d)-(f) R^2 , and (g)-(i) RMSE of the different methods.

and reflection coefficients.

By substituting (4) into (1), the general form of the forward equation in AVO theory is obtained, expressed as

$$D = W * f(m) = G(m) \quad (5)$$

where G represents the forward operator.

AVO inversion is the reverse process of AVO forward modeling. When the mapping matrix G is invertible and the influence of the seismic wavelet is disregarded, the inversion result can be expressed as

$$m = G^{-1}(D) \quad (6)$$

where G^{-1} represents the inverse operator of G . In AVO inversion, the mapping operator G^{-1} is typically non-invertible.

B. Semi-supervised seismic inversion structure

When deep learning is applied to AVO inversion, the mapping operator G^{-1} in equation (6) is replaced by a network, mathematically expressed as

$$m = \mathcal{I}_w(D) \quad (7)$$

where \mathcal{I}_w denotes the inversion network, and w denotes the trainable network parameters. The network can perform

supervised learning using well-log data, with the objective function expressed as

$$J(\mathcal{I}_w) = \min_{\mathcal{I}_w} \|\|m_l - \mathcal{I}_w(D_l)\|_2^2 \quad (8)$$

where where $\|\cdot\|_2^2$ denotes the L2 norm, m_l represents the elastic parameters from well-log and D_l denotes the labeled seismic data.

However, the proportion of well-log data is extremely small compared to the entire seismic dataset. This leads to a significant shortage of training data, which significantly affects inversion accuracy and limits the practical application of this method. To address this issue, we constructed a forward network, expressed as

$$D = \mathcal{F}_w(m) \quad (9)$$

where \mathcal{F}_w represents the forward network. For supervised training with well-log data, its objective function is

$$J(\mathcal{F}_w) = \min_{\mathcal{F}_w} \|\|D_l - \mathcal{F}_w(m_l)\|_2^2 \quad (10)$$

Moreover, to improve the generalization ability of the inversion and forward networks, we process a large amount of unlabeled seismic data (i.e., seismic data not from well

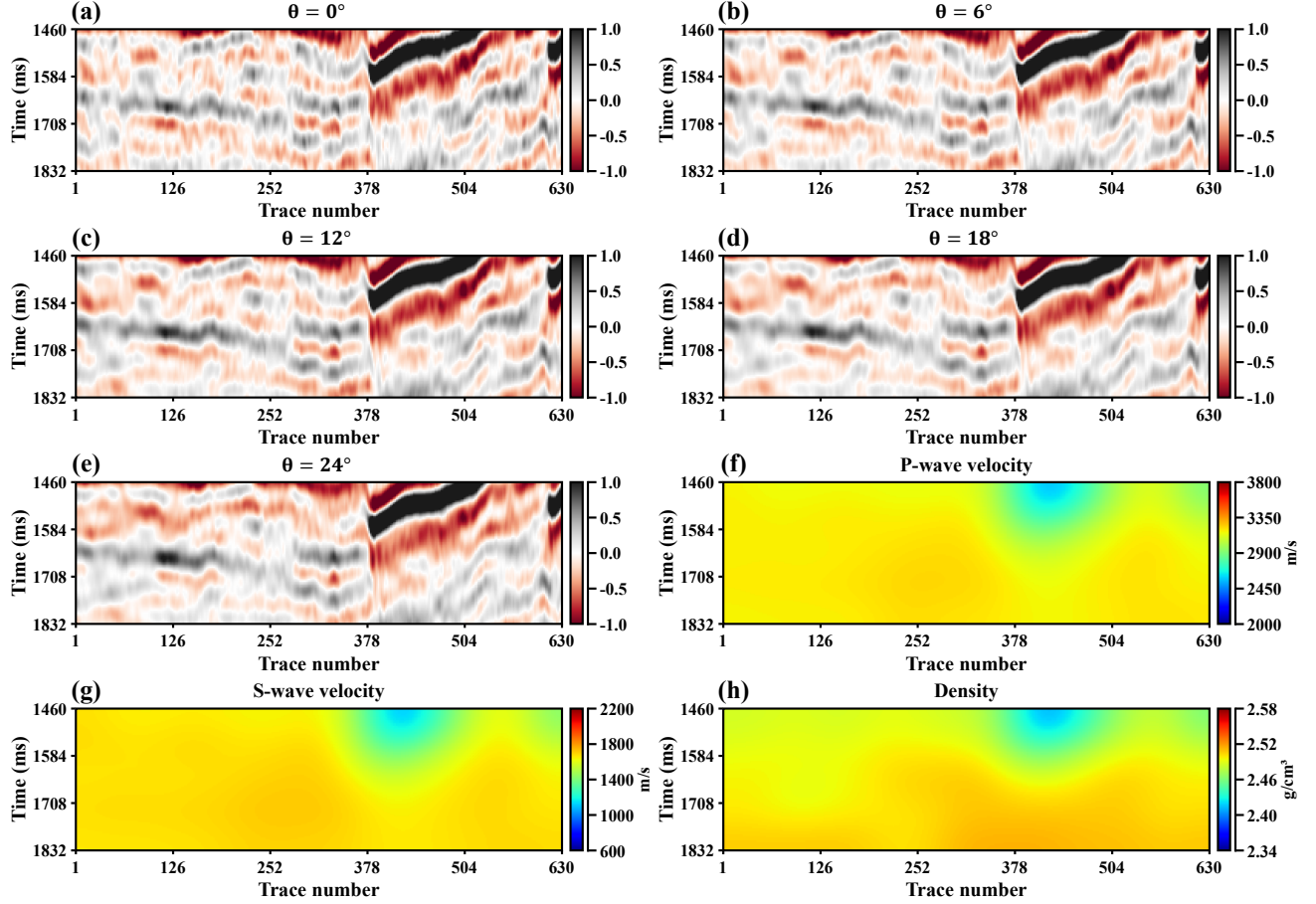


Fig. 17. Field seismic profiles of (a) 0° , (b) 6° , (c) 12° , (d) 18° , and (e) 24° . Low-frequency profile of (f) P-wave velocity, (g) S-wave velocity, and (h) density.

locations) through the inversion and forward networks. The objective function is expressed as

$$J(\mathcal{I}_w, \mathcal{F}_w) = \min_{\mathcal{I}_w, \mathcal{F}_w} \|D_u - \mathcal{F}_w(\mathcal{I}_w(D_u))\|_2^2 \quad (11)$$

where D_u represents the unlabeled seismic data. Finally, by combining equations (8), (10), and (11), the objective function is obtained:

$$\begin{aligned} J(\mathcal{I}_w, \mathcal{F}_w) = & \min_{\mathcal{I}_w} \|m_l - \mathcal{I}_w(D_l)\|_2^2 \\ & + \min_{\mathcal{F}_w} \|D_l - \mathcal{F}_w(m_l)\|_2^2 \\ & + \min_{\mathcal{I}_w, \mathcal{F}_w} \|D_u - \mathcal{F}_w(\mathcal{I}_w(D_u))\|_2^2 \end{aligned} \quad (12)$$

C. Strong spatial feature constraints

To establish the mapping of strong spatial features between the predicted parameters at well locations and those at non-well locations, we propose a strong spatial feature constraint

method. The matrix forms of m_l and $\mathcal{I}_w(D_l)$ in (11) are given by

$$\begin{aligned} m_l &= \begin{bmatrix} 0 & \cdots & m_{1+\frac{M-1}{2},1} & \cdots & 0 \\ \vdots & \ddots & \vdots & \ddots & \vdots \\ 0 & \cdots & m_{1+\frac{M-1}{2},N} & \cdots & 0 \end{bmatrix}_{N \times M} \\ \mathcal{I}_w(D_l) &= \begin{bmatrix} \hat{m}_{1,1} & \cdots & \hat{m}_{1+\frac{M-1}{2},1} & \cdots & \hat{m}_{M,1} \\ \vdots & \ddots & \vdots & \ddots & \vdots \\ \hat{m}_{1,N} & \cdots & \hat{m}_{1+\frac{M-1}{2},N} & \cdots & \hat{m}_{M,N} \end{bmatrix}_{N \times M} \end{aligned} \quad (13)$$

where \hat{m} represents the predicted parameters. It can be seen from equation (13) that the well-log label only constrains the $1 + \frac{M-1}{2}$ -th trace, which corresponds to the middle trace. To enable the well-log label to constrain adjacent traces, we define a label ablation factor, expressed as

$$R = \begin{bmatrix} 1 & \cdots & 0 & \cdots & 1 \\ \vdots & \ddots & \vdots & \ddots & \vdots \\ 1 & \cdots & 0 & \cdots & 1 \end{bmatrix}_{N \times M} \quad (14)$$

We can set the predicted parameters of the middle trace to zero by using $\hat{m} * R$. Furthermore, a strong spatial feature constraint network \mathcal{S}_w was constructed to recover the missing data of the middle trace using adjacent traces. To ensure the stable convergence of the network, the self-consistency [59], [60], [61] is introduced. The objective function is expressed as

$$J(\mathcal{S}_w) = \min_{\mathcal{S}_w} \|m_l - (\mathcal{S}_w(\hat{m}_l * R)) * (1 - R)\|_2^2 + \min_{\mathcal{S}_w} \|\hat{m}_l * R - (\mathcal{S}_w(\hat{m}_l * R)) * R\|_2^2 \quad (15)$$

By combining equations (12) and (15), the inversion objective function is obtained:

$$J(\mathcal{I}_w, \mathcal{F}_w, \mathcal{S}_w) = \min_{\mathcal{I}_w} \|m_l - \mathcal{I}_w(D_l)\|_2^2 + \min_{\mathcal{F}_w} \|D_l - \mathcal{F}_w(m_l)\|_2^2 + \min_{\mathcal{I}_w, \mathcal{F}_w} \|D_u - \mathcal{F}_w(\mathcal{I}_w(D_u))\|_2^2 + \min_{\mathcal{S}_w} \|m_l - (\mathcal{S}_w(\hat{m}_l * R)) * (1 - R)\|_2^2 + \min_{\mathcal{S}_w} \|\hat{m}_l * R - (\mathcal{S}_w(\hat{m}_l * R)) * R\|_2^2 \quad (16)$$

In addition, SSFC-SSL uses the low-frequency information of the elastic parameters as conditional input to improve the inversion accuracy. Equation (16) is written as

$$J(\mathcal{I}_w, \mathcal{F}_w, \mathcal{S}_w) = \min_{\mathcal{I}_w} \underbrace{\|m_l - \mathcal{I}_w(D_l, m_{low})\|_2^2}_{\mathcal{L}_I} + \min_{\mathcal{F}_w} \underbrace{\|D_l - \mathcal{F}_w(m_l)\|_2^2}_{\mathcal{L}_F} + \min_{\mathcal{I}_w, \mathcal{F}_w} \underbrace{\|D_u - \mathcal{F}_w(\mathcal{I}_w(D_u, m_{low}))\|_2^2}_{\mathcal{L}_{Recon}} + \min_{\mathcal{S}_w} \underbrace{\|m_l - (\mathcal{S}_w(\hat{m}_l * R)) * (1 - R)\|_2^2}_{\mathcal{L}_{SSFC}} + \min_{\mathcal{S}_w} \underbrace{\|\hat{m}_l * R - (\mathcal{S}_w(\hat{m}_l * R)) * R\|_2^2}_{\mathcal{L}_{SC}} \quad (17)$$

Therefore, the total loss of the SSFC-SSL network can be expressed as

$$Loss = \mathcal{L}_I + \mathcal{L}_F + \mathcal{L}_{SSFC} + \mathcal{L}_{Recon} + \mathcal{L}_{sc} \quad (18)$$

where \mathcal{L}_I represents the training loss of the inversion network, \mathcal{L}_F represents the training loss of the forward network, \mathcal{L}_{SSFC} represents the training loss of the SSFC network, \mathcal{L}_{Recon} represents the loss from the reconstruction of unlabeled seismic data, and \mathcal{L}_{sc} represents the self-consistency loss of the SSFC network.

D. Workflow of SSFC-SSL

The workflow of the SSFC-SSL method for AVO inversion consists of two parts: training and prediction. During the training phase, the SSFC-SSL method requires the simultaneous training of the forward-modeling network, the inversion network, and the SSFC network, thereby achieving closed-loop optimization among all three.

Before starting the training, we initialize the weights and biases of the neural networks. The data include labeled, unlabeled seismic data, and well-log elastic parameters (P-wave velocity, S-wave velocity, and density). Additionally, a low-frequency model is integrated into the network, alongside the seismic data, as prior information. During training, labeled seismic data is used to optimize the forward and inversion networks. During the training process, both labeled and unlabeled seismic data are utilized to optimize the inversion and forward networks. The output of the forward network is fed back to the inversion network in the form of pseudo-labels, enabling the effective utilization of unlabeled data. Meanwhile, well-log elastic parameters contribute to the optimization of the inversion network, forward network, and SSFC network. Eventually, a mapping between multi-trace seismic data and multi-trace elastic parameters is achieved. During the prediction stage, the SSFC network and the forward network are no longer involved, and the inversion task is completed solely by leveraging the efficient inference capability of the inversion network.

E. Network structure

The SSFC-SSL consists of three sub-networks: the inversion network, the forward network, and the strong spatial feature constraints network. To accomplish the inversion task, we adopted the CNN as the basic architecture. Given the need to extract global features from the shallow structure in the inversion network, which requires a larger receptive field, we introduced temporal convolutional networks (TCN) and a dilated convolution design. Dilated convolution allows for precise control of the receptive field by introducing a dilation factor, enabling the network to achieve a larger receptive field with fewer layers, thereby capturing historical information over a longer time scale. Fig. 3 shows an example of the 5x5 dilated convolution kernel structure, with an initial receptive field of 5. By introducing dilation factors of 2 and 3, the receptive fields for a single-layer network are expanded to 11 and 17, respectively. The dilated convolution significantly enhances the ability of the network to extract shallow global features and reduces the parameter count.

Fig. 4 illustrates the inversion network, consisting of four TCN blocks and three CNN blocks, K is the number of seismic profiles corresponding to different incidence angles. The structure of the TCN, shown within the dashed box in Fig. 4, consists of two branches. The first branch transforms the input, while the second applies a 1×1 convolution operation. Then, the outputs of the two branches are added together to generate the final result. The residual connection enables information to flow across layers, effectively preventing the loss of information due to excessive depth. Compared to Recurrent Neural Networks (RNNs), the TCN addresses the issues of vanishing and exploding gradients. Figs. 5 and 6 illustrate the structures of the forward network and the SSFC network, both of which consist of four convolutional layers, each followed by a Batch Normalization (BN) layer and a ReLU activation layer. The two network structures are designed to maintain consistency.

TABLE II
QUANTITATIVE ANALYSIS OF THE INVERSION RESULTS FOR THE SYNTHETIC DATA.

Method	P-wave Velocity			S-wave Velocity			Density		
	PCC	R ²	RMSE	PCC	R ²	RMSE	PCC	R ²	RMSE
Model-Based	0.9731	0.9447	0.0757	0.9715	0.9402	0.1291	0.8478	0.6754	0.0437
1D-SL	0.9692	0.9172	0.0777	0.9680	0.9143	0.1288	0.9491	0.8831	0.0231
1D-SSL	0.9786	0.9467	0.0654	0.9775	0.9442	0.1093	0.9597	0.9049	0.0215
2D-SSL	0.9846	0.9669	0.0553	0.9863	0.9637	0.0832	0.9751	0.9403	0.0166
SSFC-SSL	0.9911	0.9814	0.0420	0.9892	0.9779	0.0624	0.9868	0.9617	0.0123

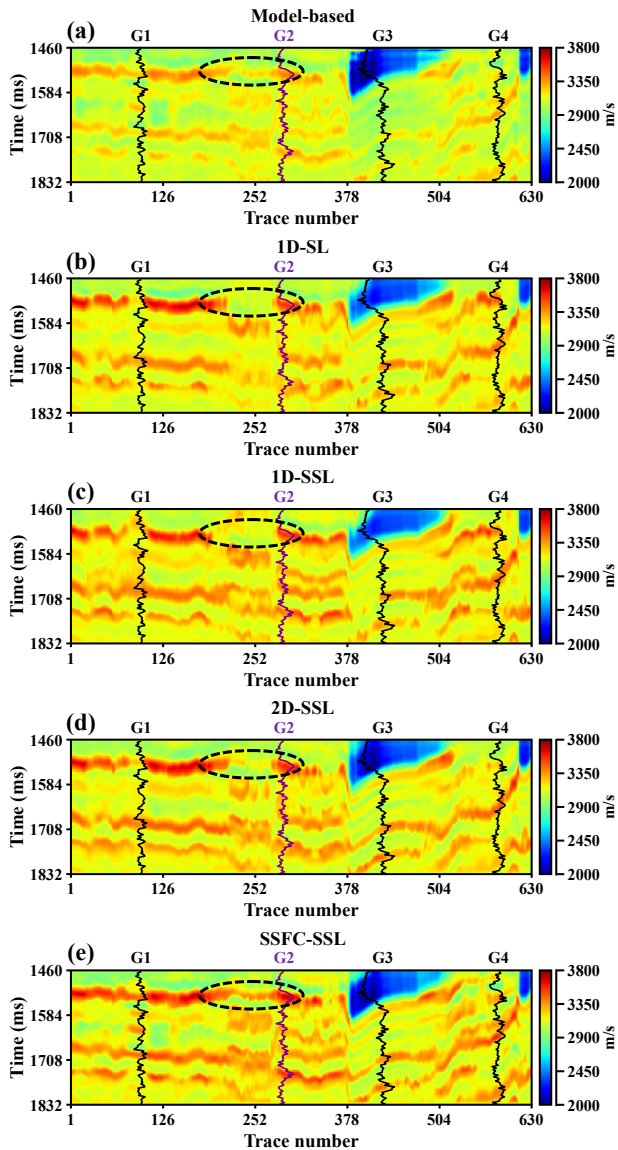


Fig. 18. Inversion results of P-wave velocity using (a) model-based, (b) 1D-SL, (c) 1D-SSL, (d) 2D-SSL, and (e) SSFC-SSL methods.

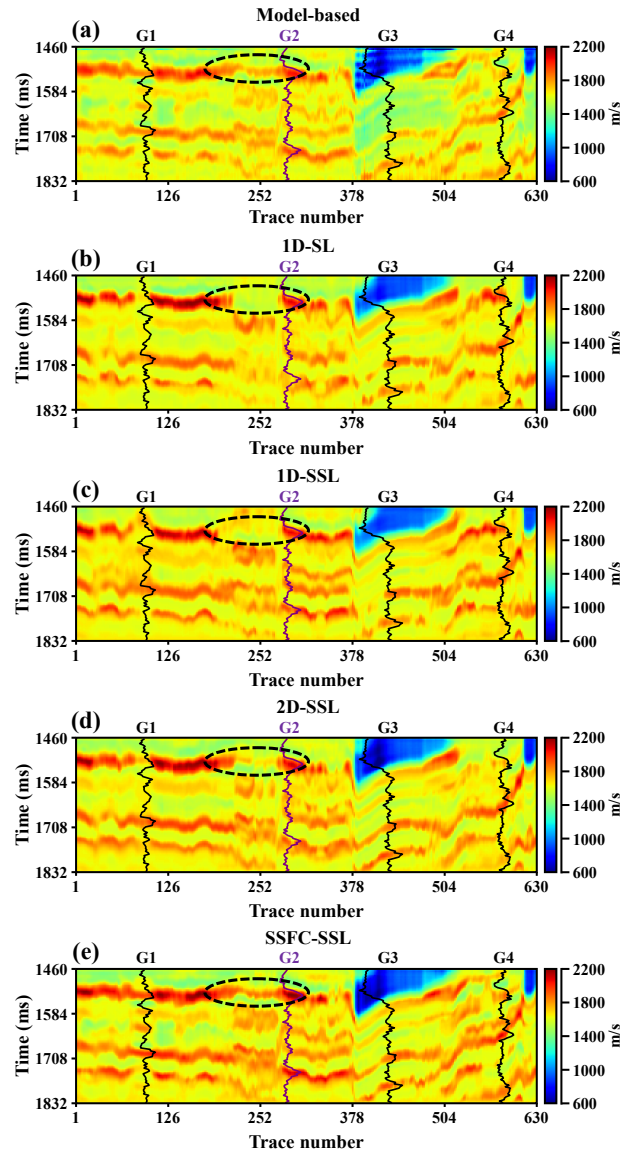


Fig. 19. Inversion results of S-wave velocity using (a) model-based, (b) 1D-SL, (c) 1D-SSL, (d) 2D-SSL, and (e) SSFC-SSL methods.

III. EXPERIMENTS

A. Performance metrics and hyperparameter.

In the experiment, to ensure the stable convergence of the network, we normalized the data using the following

equations:

$$m' = \frac{m - \mu_m}{\sigma_m} \quad (19)$$

$$D' = \frac{D - \mu_D}{\sigma_D} \quad (20)$$

TABLE III
QUANTITATIVE ANALYSIS OF THE INVERSION RESULTS FOR THE FIELD DATA.

Method	P-wave Velocity			S-wave Velocity			Density		
	PCC	R ²	RMSE	PCC	R ²	RMSE	PCC	R ²	RMSE
Model-Based	0.7979	0.7582	0.0348	0.7512	0.6948	0.0672	0.5176	0.4266	0.0155
1D-SL	0.8738	0.8203	0.0297	0.8767	0.7751	0.0485	0.8211	0.7401	0.0073
1D-SSL	0.9003	0.8496	0.0253	0.8868	0.7942	0.0416	0.8717	0.7650	0.0049
2D-SSL	0.9294	0.8652	0.0205	0.9103	0.8454	0.0316	0.9227	0.8516	0.0037
SSFC-SSL	0.9478	0.8981	0.0130	0.9181	0.8698	0.0202	0.9450	0.8838	0.0031

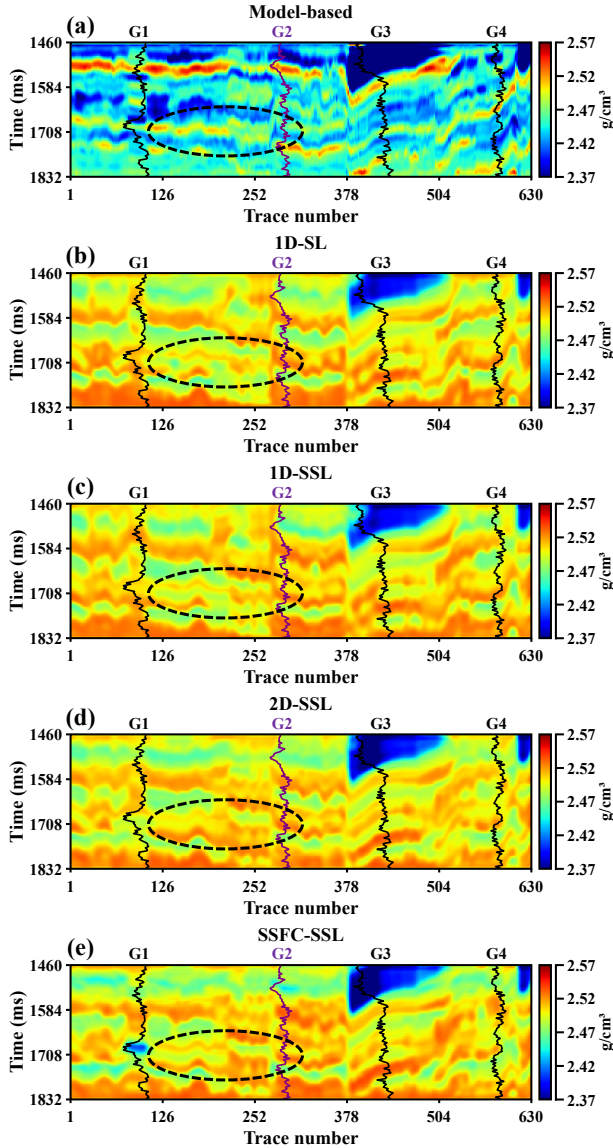


Fig. 20. Inversion results of density using (a) model-based, (b) 1D-SL, (c) 1D-SSL, (d) 2D-SSL, and (e) SSFC-SSL methods.

where m and D represent the original seismic data and the original model (or low-frequency model), μ_m and μ_D represent the mean of m and D , and σ_M and σ_D represent the variance of m and D . m' and D' denote the normalized model (or low-frequency model) and the seismic data. It is important to note that m includes V_P , V_S , and ρ , which have different

dimensions, so each parameter is normalized separately.

To quantify the accuracy of the inversion results, we introduced the Pearson correlation coefficient (PCC), coefficient of determination (R^2), and root mean square error (RMSE). PCC is a measure of the linear relationship between two variables, quantifying the strength and direction of their correlation. It is defined as

$$\text{PCC} = \frac{\sum_{k=1}^n (m_k - \mu_m)(\hat{m}_k - \mu_{\hat{m}})}{\sqrt{\sum_{k=1}^n (y_k - \mu_m)^2} \sqrt{\sum_{k=1}^n (\hat{m}_k - \mu_{\hat{m}})^2}} \quad (21)$$

where m_k is the k th true value, \hat{m}_k represents the k th predicted value, μ_m and $\mu_{\hat{m}}$ are the mean values of the input parameters and predicted values, respectively, and n denotes the number of data points. The R^2 score is a statistical indicator used to measure the prediction effect of a regression model, representing the degree to which the model explains the total variation of the target variable. Its value ranges from 0 to 1, and the closer the R^2 score is to 1, the closer the prediction results are to the true values. The definition of R^2 is

$$R^2 = 1 - \frac{\sum_{k=1}^n (m_k - \hat{m}_k)^2}{\sum_{k=1}^n (m_k - \mu_m)^2} \quad (22)$$

The RMSE was obtained by taking the square root of the mean-square error (MSE), which is a measure of the difference between the predicted value and the true value. The RMSE can be formulated as

$$\text{RMSE} = \sqrt{\frac{1}{n} \sum_{k=1}^n (m_k - \hat{m}_k)^2} \quad (23)$$

For network training, we set a series of hyperparameters, as listed in Table I. Additionally, the number of multi-traces was set to 5. The experiment was conducted on a computer running the Windows 11 operating system, with a configuration that included 32GB of RAM, an Intel Core i5-12490F processor, and an NVIDIA GeForce GTX 3060 Graphics Processing Unit (GPU) with 8GB of video memory. The experimental platform used was PyTorch [62].

B. Testing on Marmousi2 model

To verify the effectiveness of the SSFC-SSL method, we used the Marmousi2 model data for inversion tests. This model includes 2720 common depth points (CDPs) and 600 sampling points, with a sampling interval of 2 ms. Reflection coefficients were calculated from the model using (2) and convolved with a zero-phase Ricker wavelet of 20 Hz dominant frequency. As shown in Fig. 7(a)-(e), five sets of seismic data with incident

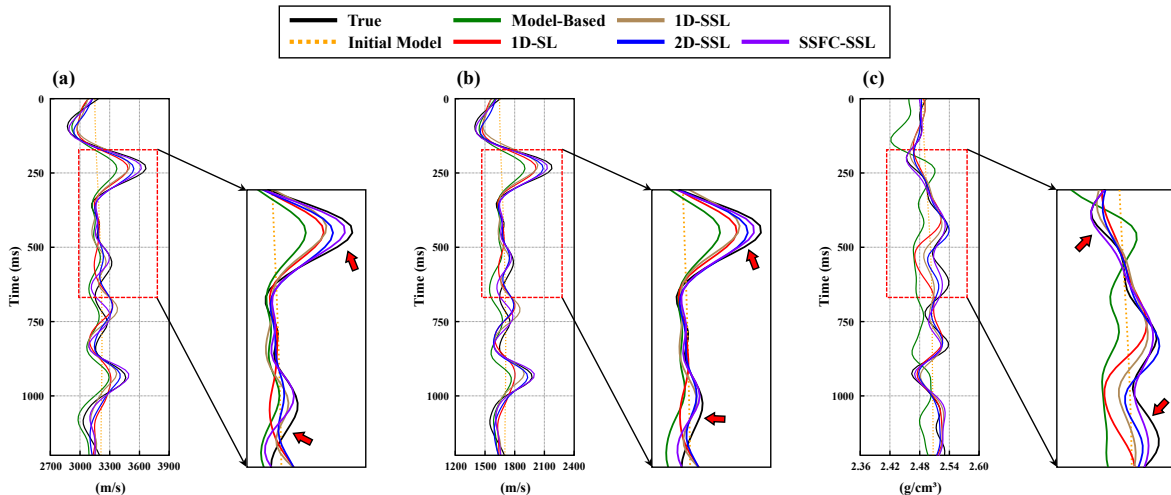


Fig. 21. Inversion results of (a) P-wave velocity, (b) S-wave velocity, and (c) density at well G2.

angles ranging from 0 to 24 degrees (at equal intervals) were synthesized as input. Additionally, a low-pass filter was applied to the model data to obtain the low-frequency model, which is shown in Fig. 7(f)-(h). As shown in Fig. 8, we extracted 18 traces at equal intervals to construct the labeled dataset, which accounted for only 0.66% of the total traces. The remaining traces were randomly sampled at an interval of 50 traces as the unlabeled data. Fig. 9 shows the loss curves of SSFC-SSL, and all losses can converge stably.

To assess the effectiveness of the proposed method, we compared it with one-dimensional supervised learning (1D-SL), one-dimensional semi-supervised learning (1D-SSL), and two-dimensional semi-supervised learning (2D-SSL) methods. Additionally, we used the commonly used model-driven BFGS method as a benchmark. Fig. 10 shows the inversion results for different methods. Model-based methods can display the stratigraphic structure, but their resolution is slightly low. The 1D-SL method improves inversion resolution but brings noticeable vertical artifacts. Although the 1D-SSL method reduces these artifacts to some degree, it is still blurred at the rock layer unconformities, as shown by the elliptical wireframes in Fig. 10. The 2D-SSL and SSFC-SSL methods improve lateral continuity in the inversion results. Compared to the 2D-SSL method, the SSFC-SSL method offers clearer delineation at the boundaries of thin layers (red arrows, Fig. 10(n)-(o)). Fig. 11 shows the residuals between the inversion results of each method and the true values. The SSFC-SSL method exhibits low errors in both the reservoir and complex geological structures (red and blue rectangular boxes). Fig. 12 shows the prediction results for trace 600 not included in the training data. By comparing the inversion results with the measured 2D profile and 1D trace, it is evident that the SSFC-SSL method yields more accurate results (indicated by the red arrow). Despite the extreme complexity of the structural features and significant lithological changes at depths of 620 ms, the inversion results using the SSFC-SSL method maintain high accuracy and resolution. To quantitatively compare the

accuracy of each method, we calculated the mean values of the inversion profiles using PCC, R^2 , and RMSE. The results are listed in Table II. The SSFC-SSL method achieved the best values in all indicators.

In practical applications, the number of available well-log labels is often limited due to complex geological conditions and high well-log costs. Therefore, we further designed a comparison of various methods under the condition of scarce labels. As shown in Fig. 13, we sampled seven and three training traces at equal intervals, which represent only 0.26% and 0.11% of the total number of traces, respectively. Figs. 14 and 15 show the inversion results using seven and three training traces, respectively. As the number of training traces decreases, the vertical artifacts of the 1D-SL and 1D-SSL methods become significantly more severe. Although the 2D-SSL method improves lateral continuity, it still exhibits numerous high-value errors in complex strata (see the areas marked by the elliptical box). In contrast, the SSFC-SSL method maintains high accuracy and resolution by fully considering the relationships between adjacent traces. Fig. 16 shows the quantitative comparison of different inversion methods. By comparison, we can see that the SSFC-SSL method achieves higher PCC and R^2 values, along with a low RMSE. This verifies the efficiency and accuracy of the proposed method under limited well-log labels.

C. Testing on field data

To verify the practicality of the SSFC-SSL method, we applied it to field data from the South China Sea. The main rock types in the field data are sandstone and mudstone, which feature complex lithology, significant thickness variations, and strong heterogeneity. Therefore, high accuracy and resolution of velocity and density are essential. We selected a line consisting of 630 common depth points (CDPs), passing through well G1 (CDP = 98), well G2 (CDP = 304), well G3 (CDP = 443), and well G4 (CDP = 615). Wells G1,

G2, and G3 were used for training, while well G3 was used to evaluate the inversion results. Before inversion, the seismic data were processed using noise suppression, surface-consistent deconvolution, amplitude recovery, and resampling to improve the signal-to-noise ratio and resolution. The low-frequency information of the different elastic parameters is obtained by layer interpolation, extrapolation, and smoothing of the corresponding well-log curves. The seismic data for different angles are shown in Fig. 17, and the low-frequency profiles of P-wave velocity, S-wave velocity, and density are shown in Fig. 18. The hyperparameters were the same as those used in the synthetic data experiments.

We performed AVO inversion on field data using the model-based, 1D-SL, 1D-SSL, 2D-SSL, and SSFC-SSL methods, and the results are shown in Figs. 18, 19, and 20. The model-based method and conventional DL-based methods effectively uncover stratigraphic features. However, they have limitations in resolution, particularly in the accuracy of density inversion. In contrast, the elastic parameters obtained using the SSFC-SSL method exhibit higher resolution and better lateral continuity, as indicated by the elliptically labeled regions. To achieve a further comparison, the model-based method and the DL-based method results at the location of the blind well G2 are shown in Fig. 21. Table III shows the PCC, R^2 , and SSIM values between the inversion results at the well G2 and the well-log curves. The inversion results of SSFC-SSL can fit the well-log curves well, especially in the area indicated by the arrows.

IV. CONCLUSION

In this article, we introduce the SSFC-SSL method, a novel approach to AVO inversion that addresses the limitations of traditional one-dimensional and two-dimensional DL methods. Unlike one-dimensional DL methods, which suffer from a lack of lateral continuity, and two-dimensional DL methods, which fail to fully utilize well-log data, SSFC-SSL overcomes these challenges by integrating a label annihilation operator and a strong spatial feature constraints (SSFC) network. This approach effectively constrains both well-log data and adjacent seismic traces, thereby improving both lateral continuity and inversion accuracy. Experimental results on both synthetic data and field data show that the SSFC-SSL method is superior to the model-based, one-dimensional DL, and two-dimensional DL methods in terms of lateral continuity and inversion accuracy. In future work, we plan to extend the SSFC-SSL method to post-stack inversion, aiming to further enhance the precision of seismic parameter estimation.

REFERENCES

- [1] J. L. Simmons Jr and M. M. Backus, "Waveform-based avo inversion and avo prediction-error," *Geophysics*, vol. 61, no. 6, pp. 1575–1588, 1996.
- [2] W. Alemlie and M. D. Sacchi, "High-resolution three-term avo inversion by means of a trivariate cauchy probability distribution," *Geophysics*, vol. 76, no. 3, pp. R43–R55, 2011.
- [3] J. Meng, S. Wang, W. Cheng, Z. Wang, and L. Yang, "Avo inversion based on transfer learning and low-frequency model," *IEEE Geoscience and Remote Sensing Letters*, vol. 19, pp. 1–5, 2021.
- [4] K. Zoeppritz, "On the reflection and propagation of seismic waves," *Göttinger Nachrichten*, vol. 1, no. 5, pp. 66–84, 1919.
- [5] R. Bortfeld, "Approximations to the reflection and transmission coefficients of plane longitudinal and transverse waves," *Geophysical Prospecting*, vol. 9, no. 4, pp. 485–502, 1961.
- [6] K. Aid and P. Richards, "Quantitative seismology: Theory and methods," *San Francisco*, 1980.
- [7] R. Shuey, "A simplification of the Zoeppritz equations," *Geophysics*, vol. 50, no. 4, pp. 609–614, 1985.
- [8] G. Smith and P. Gidlow, "Weighted stacking for rock property estimation and detection of gas," *Geophysical prospecting*, vol. 35, no. 9, pp. 993–1014, 1987.
- [9] B. Goodway, T. Chen, and J. Downton, "Improved avo fluid detection and lithology discrimination using lamé petrophysical parameters; " $\lambda\rho$ ", " $\mu\rho$ ", & " $\lambda\mu$ fluid stack", from p and s inversions," in *SEG technical program expanded abstracts 1997*. Society of Exploration Geophysicists, 1997, pp. 183–186.
- [10] D. Gray and E. Andersen, "The application of avo and inversion to the estimation of rock properties," in *SEG International Exposition and Annual Meeting*. SEG, 2000, pp. SEG–2000.
- [11] L. Ikelle, "Linearized inversion of 3-d multi-offset data: Background reconstruction and avo inversion," *Geophysical Journal International*, vol. 123, no. 2, pp. 507–528, 1995.
- [12] J. E. Downton and C. Ursenbach, "Linearized amplitude variation with offset (avo) inversion with supercritical angles," *Geophysics*, vol. 71, no. 5, pp. E49–E55, 2006.
- [13] X.-Y. Yin, W. Deng, and Z.-Y. Zong, "Avo inversion based on inverse operator estimation in trust region," *Journal of Geophysics and Engineering*, vol. 13, no. 2, pp. 194–206, 2016.
- [14] B. She, Y. Wang, J. Zhang, J. Wang, and G. Hu, "Avo inversion with high-order total variation regularization," *Journal of Applied Geophysics*, vol. 161, pp. 167–181, 2019.
- [15] Z.-Y. Zong, X.-Y. Yin, and K. Li, "Joint avo inversion in the time and frequency domain with bayesian interference," *Applied Geophysics*, vol. 13, no. 4, pp. 631–640, 2016.
- [16] K. Li, K. Li, X. Yin, and Z. Zong, "Hierarchical bayesian probabilistic seismic avo inversion using gibbs sampling with ia2rms algorithm," *IEEE Geoscience and Remote Sensing Letters*, vol. 19, pp. 1–5, 2022.
- [17] E. H. Jensen, T. A. Johansen, P. Avseth, and K. Bredesen, "Quantitative interpretation using inverse rock-physics modeling on avo data," *The Leading Edge*, vol. 35, no. 8, pp. 677–683, 2016.
- [18] S. Misra and M. D. Sacchi, "Global optimization with model-space preconditioning: Application to avo inversion," *Geophysics*, vol. 73, no. 5, pp. R71–R82, 2008.
- [19] N. Ahmed, W. W. Weibull, and D. Grana, "Constrained non-linear avo inversion based on the adjoint-state optimization," *Computers & Geosciences*, vol. 168, p. 105214, 2022.
- [20] N. Ahmed, W. W. Weibull, B. Quintal, D. Grana, and T. Bhakta, "Frequency-dependent avo inversion applied to physically based models for seismic attenuation," *Geophysical Journal International*, vol. 233, no. 1, pp. 234–252, 2023.
- [21] W. Feng, Y. Liu, Y. Li, H. Li, and X. Wang, "Acoustic impedance prediction using an attention-based dual-branch double-inversion network," *Earth Science Informatics*, vol. 18, no. 1, pp. 1–20, 2025.
- [22] P. Avseth, A. Janke, and F. Horn, "Avo inversion in exploration—key learnings from a norwegian sea prospect," *The Leading Edge*, vol. 35, no. 5, pp. 405–414, 2016.
- [23] Q. Du and H. Yan, "Pp and ps joint avo inversion and fluid prediction," *Journal of Applied Geophysics*, vol. 90, pp. 110–118, 2013.
- [24] Z. Li, X. Chen, J. Li, and J. Zhang, "Pertinent multigate mixture-of-experts-based prestack three-parameter seismic inversion," *IEEE Transactions on Geoscience and Remote Sensing*, vol. 60, pp. 1–15, 2022.
- [25] L. Niu, J. Geng, X. Wu, L. Zhao, and H. Zhang, "Data-driven method for an improved linearised avo inversion," *Journal of Geophysics and Engineering*, vol. 18, no. 1, pp. 1–22, 2021.
- [26] J. Zhang, H. Sun, G. Zhang, and X. Zhao, "Deep learning seismic inversion based on prestack waveform datasets," *IEEE Transactions on Geoscience and Remote Sensing*, vol. 60, pp. 1–11, 2022.
- [27] F. Yang and J. Ma, "Deep-learning inversion: A next-generation seismic velocity model building method," *Geophysics*, vol. 84, no. 4, pp. R583–R599, 2019.
- [28] H. WANG, J.-y. YAN, G.-m. FU, and X. WANG, "Current status and application prospect of deep learning in geophysics," *Progress in Geophysics*, vol. 35, no. 2, pp. 642–655, 2020.
- [29] W. Chen, L. Yang, B. Zha, M. Zhang, and Y. Chen, "Deep learning reservoir porosity prediction based on multilayer long short-term memory network," *Geophysics*, vol. 85, no. 4, pp. WA213–WA225, 2020.

- [30] M. Masroor, M. E. Niri, and M. H. Sharifinasab, "A multiple-input deep residual convolutional neural network for reservoir permeability prediction," *Geoenergy Science and Engineering*, vol. 222, p. 211420, 2023.
- [31] W. Xiong, X. Ji, Y. Ma, Y. Wang, N. M. AlBinHassan, M. N. Ali, and Y. Luo, "Seismic fault detection with convolutional neural network," *Geophysics*, vol. 83, no. 5, pp. O97–O103, 2018.
- [32] S. Wang, X. Si, Z. Cai, L. Sun, W. Wang, and Z. Jiang, "Fast global self-attention for seismic image fault identification," *IEEE Transactions on Geoscience and Remote Sensing*, 2024.
- [33] Z. Liao, Y. Li, E. Xia, Y. Liu, and R. Hu, "A twice denoising autoencoder framework for random seismic noise attenuation," *IEEE Transactions on Geoscience and Remote Sensing*, vol. 61, pp. 1–15, 2023.
- [34] Y. Zhao, Y. Li, X. Dong, and B. Yang, "Low-frequency noise suppression method based on improved dncnn in desert seismic data," *IEEE Geoscience and Remote Sensing Letters*, vol. 16, no. 5, pp. 811–815, 2018.
- [35] H. Di, Z. Li, H. Maniar, and A. Abubakar, "Seismic stratigraphy interpretation by deep convolutional neural networks: A semisupervised workflow," *Geophysics*, vol. 85, no. 4, pp. WA77–WA86, 2020.
- [36] X. Gu, W. Lu, Y. Li, and Y. Wang, "Semi-supervised seismic stratigraphic interpretation constrained by spatial structure," *IEEE Transactions on Geoscience and Remote Sensing*, vol. 61, pp. 1–10, 2023.
- [37] V. Das, A. Pollack, U. Wollner, and T. Mukerji, "Convolutional neural network for seismic impedance inversion," *Geophysics*, vol. 84, no. 6, pp. R869–R880, 2019.
- [38] A. Mustafa, M. Alfarraj, and G. AlRegib, "Estimation of acoustic impedance from seismic data using temporal convolutional network," in *SEG technical program expanded abstracts 2019*. Society of Exploration Geophysicists, 2019, pp. 2554–2558.
- [39] D. Cao, P. An, and S. Liu, "Elastic-parameters inversion from ei based on the deep-learning method," in *SEG Technical Program Expanded Abstracts 2018*. Society of Exploration Geophysicists, 2018, pp. 640–644.
- [40] J. Zhang, J. Li, X. Chen, Y. Li, G. Huang, and Y. Chen, "Robust deep learning seismic inversion with a priori initial model constraint," *Geophysical Journal International*, vol. 225, no. 3, pp. 2001–2019, 2021.
- [41] S. Li, B. Liu, Y. Ren, Y. Chen, S. Yang, Y. Wang, and P. Jiang, "Deep-learning inversion of seismic data," *arXiv preprint arXiv:1901.07733*, 2019.
- [42] Y. Zheng, Q. Zhang, A. Yusifov, and Y. Shi, "Applications of supervised deep learning for seismic interpretation and inversion," *The Leading Edge*, vol. 38, no. 7, pp. 526–533, 2019.
- [43] M. Alfarraj and G. AlRegib, "Semisupervised sequence modeling for elastic impedance inversion," *Interpretation*, vol. 7, no. 3, pp. SE237–SE249, 2019.
- [44] Y. Liu, Y. Li, H. Li, J. Peng, Z. Liao, and W. Feng, "The nash-ml-stcn for prestack three-parameter inversion," *arXiv preprint arXiv:2407.00684*, 2024.
- [45] A. Navon, A. Shamsian, I. Achituv, H. Maron, K. Kawaguchi, G. Chechik, and E. Fetaya, "Multi-task learning as a bargaining game," *arXiv preprint arXiv:2202.01017*, 2022.
- [46] J. Sun, K. A. Innanen, and C. Huang, "Physics-guided deep learning for seismic inversion with hybrid training and uncertainty analysis," *Geophysics*, vol. 86, no. 3, pp. R303–R317, 2021.
- [47] R. Biswas, M. K. Sen, V. Das, and T. Mukerji, "Prestack and post-stack inversion using a physics-guided convolutional neural network," *Interpretation*, vol. 7, no. 3, pp. SE161–SE174, 2019.
- [48] Q. Ge, H. Cao, Z. Yang, S. Yuan, and C. Song, "Deep learning-based pre-stack seismic inversion constrained by avo attributes," *IEEE Geoscience and Remote Sensing Letters*, 2024.
- [49] A. Adler, M. Araya-Polo, and T. Poggio, "Deep recurrent architectures for seismic tomography," in *81st EAGE conference and exhibition 2019*, vol. 2019, no. 1. European Association of Geoscientists & Engineers, 2019, pp. 1–5.
- [50] R. Guo, J. Zhang, D. Liu, Y. Zhang, and D. Zhang, "Application of bi-directional long short-term memory recurrent neural network for seismic impedance inversion," in *81st EAGE Conference and Exhibition 2019*, vol. 2019, no. 1. European Association of Geoscientists & Engineers, 2019, pp. 1–5.
- [51] G. Fabien-Ouellet and R. Sarkar, "Seismic velocity estimation: A deep recurrent neural-network approach," *Geophysics*, vol. 85, no. 1, pp. U21–U29, 2020.
- [52] S. Yuan, X. Jiao, Y. Luo, W. Sang, and S. Wang, "Double-scale supervised inversion with a data-driven forward model for low-frequency impedance recovery," *Geophysics*, vol. 87, no. 2, pp. R165–R181, 2022.
- [53] S. Shi, M. Li, J. Wang, W. Chang, L. Li, and D. Xie, "Seismic impedance inversion based on semi-supervised learning," *Computers & Geosciences*, vol. 182, p. 105497, 2024.
- [54] Z. Wang, S. Wang, C. Zhou, and W. Cheng, "Avo inversion based on closed-loop multitask conditional wasserstein generative adversarial network," *IEEE Transactions on Geoscience and Remote Sensing*, vol. 61, pp. 1–13, 2023.
- [55] X. Wu, S. Yan, Z. Bi, S. Zhang, and H. Si, "Deep learning for multidimensional seismic impedance inversion," *Geophysics*, vol. 86, no. 5, pp. R735–R745, 2021.
- [56] Q. Wang, Y. Wang, Y. Ao, and W. Lu, "Seismic inversion based on 2d-cnns and domain adaption," *IEEE Transactions on Geoscience and Remote Sensing*, vol. 60, pp. 1–12, 2022.
- [57] A. Mustafa, M. Alfarraj, and G. AlRegib, "Joint learning for spatial context-based seismic inversion of multiple data sets for improved generalizability and robustness," *Geophysics*, vol. 86, no. 4, pp. O37–O48, 2021.
- [58] K. Li, Y. Dou, Y. Xiao, R. Jing, J. Zhu, and C. Ma, "Transinver: 3d data-driven seismic inversion based on self-attention," *Geophysics*, vol. 89, no. 1, pp. WA127–WA141, 2024.
- [59] F. Pourpanah, M. Abdar, Y. Luo, X. Zhou, R. Wang, C. P. Lim, X.-Z. Wang, and Q. J. Wu, "A review of generalized zero-shot learning methods," *IEEE transactions on pattern analysis and machine intelligence*, vol. 45, no. 4, pp. 4051–4070, 2022.
- [60] X. Wang, J. Wei, D. Schuurmans, Q. Le, E. Chi, S. Narang, A. Chowdhery, and D. Zhou, "Self-consistency improves chain of thought reasoning in language models," *arXiv preprint arXiv:2203.11171*, 2022.
- [61] J. Peng, Y. Liu, M. Wang, Y. Li, and H. Li, "Zero-shot self-consistency learning for seismic irregular spatial sampling reconstruction," *arXiv preprint arXiv:2411.00911*, 2024.
- [62] A. Paszke, S. Gross, F. Massa, A. Lerer, J. Bradbury, G. Chanan, T. Killeen, Z. Lin, N. Gimelshein, L. Antiga *et al.*, "Pytorch: An imperative style, high-performance deep learning library," *Advances in neural information processing systems*, vol. 32, 2019.